A Journal of the Gesellschaft Deutscher Chemiker

Angewandte International Edition GDCh Chemie

www.angewandte.org

Accepted Article

Title: Modulating Spin State of Ni Single Atomic Center for High-Performance Electrocatalytic Carbon Dioxide Reduction

Authors: Shuang-Quan Zang, Zhen Chen, Jiankang Liu, Jianpeng Li, Yueteng Zhang, Jia Yang, Jun Li, Zhiyuan Wang, and Zhongyi Liu

To be cited as: *Angew. Chem. Int. Ed.* **2025**, e202506845

Link to VoR: https://doi.org/10.1002/anie.202506845

WILEY VCH

Modulating Spin State of Ni Single Atomic Center for High-Performance Electrocatalytic Carbon Dioxide Reduction

Zhen Chen,[†] Jiankang Liu,[†] Jianpeng Li,[†] Yueteng Zhang, Jia Yang, Jun Li, Zhiyuan Wang,* Zhongyi Liu, Shuang-Quan Zang*

Z. Chen, J. Liu, J. Li, Prof. J. Li, Prof. Z. Wang

Henan Institute of Advanced Technology, State Key Laboratory of Coking Coal Resources Green Exploitation, and College of Chemistry, Zhengzhou University, Zhengzhou 450001, China.

E-mail: wangzhiy@zzu.edu.cn

Dr. Y. Zhang

The Pathophysiology Department, School of Basic Medical Sciences, Cancer Chemoprevention International Collaboration Laboratory, Zhengzhou University, Zhengzhou 450001, China.

Prof. J. Yang

Institutes of Physical Science and Information Technology, Anhui University, Hefei 230601, China.

Prof. Z. Liu

State Key Laboratory of Coking Coal Resources Green Exploitation, and College of Chemistry, Zhengzhou University, Zhengzhou 450001, China

E-mail: liuzhongyi@zzu.edu.cn

Prof. S.-Q. Zang

Henan Key Laboratory of Crystalline Molecular Functional Materials, and College of Chemistry, Zhengzhou University, Zhengzhou 450001, China

E-mail: zangsqzg@zzu.edu.cn

[†]These authors contributed equally to this work.

Keywords: single atom catalyst, spin state modulation, coordination structure, electrocatalysis, CO_2 reduction

Single atom catalysts (SACs) have been widely investigated and regarded as the promising electrocatalysts for carbon dioxide reduction. However, studies on the impact of coordinated-nitrogen species in active center on the spin state and catalytic activity remain scarce. Herein, two single Ni atom electrocatalysts with distinct pyridinic-N and pyrrolic-N coordination through a rapid joule-heating method that preserves precursor nitrogen configurations. Magnetic susceptibility measurements reveal that pyridinic-N induces a high-spin state in Ni centers, while pyrrolic-N stabilizes a low-spin configuration. The high-spin Ni-$N_{pyridinic}$-C demonstrates an exceptional performance in electrocatalytic CO_2 reduction, achieving 98.8 % CO Faradaic efficiency in H-cells and maintaining >99 % Faradaic efficiency at industrial current densities (≥250 mA cm^{-2}) across alkaline, neutral, and acidic electrolytes in a gas-diffusion flow cell. A maximum power density of 1.89 mW/cm^2 and excellent charge-discharge cyclability also achieve in zinc-CO_2 battery, further demonstrating the applicability of Ni-$N_{pyridinic}$-C. Theoretical calculations demonstrate that the high-spin state enhances d-orbital dispersion, strengthening hybridization with π* orbital of CO_2 and stabilizing *COOH intermediates, thereby accelerating CO_2 activation. This study not only establishes a novel strategy for spin-state engineering through coordination control but also advances scalable electrocatalyst design for efficient carbon cycling.

10.1002/anie.202506845

1. Introduction

Electrocatalytic converting carbon dioxide into valuable chemicals and synthetic fuels under relatively benign conditions represents a promising approach to mitigating atmospheric CO_2 concentrations while providing valuable raw materials.[1] Nevertheless, the inherent high thermodynamic and kinetic stability of CO_2 necessitates the surmounting of substantial energy barriers, often accompanied by significant overpotentials.[2] Furthermore, in aqueous electrolytes, the competing hydrogen evolution reaction usually exhibits faster kinetics compared to CO_2 reduction, ultimately compromising product selectivity.[3] Consequently, design and development of ideal electrocatalysts for CO_2 reduction with excellent activity and high durability are crucial for the realization of carbon cycle.

Among the numerous electrocatalysts developed for CO_2 reduction, single atom catalysts that anchored on nitrogen-doped carbon have been widely developped and demonstrated great potential in various reactions due to their various advantages such as approximately 100% metal atom utilization and unique electronic structures, which combine the advantages of homogeneous and heterogeneous catalysts.[4] Both theoretical calculations and experimental results in recent decades have confirmed that the active sites in single atom catalysts are M-N_xC moieties, whose spin state play a crucial role in determining the intrinsic activity of single atom catalysts. The spin state of the single-atom active center is determined by the occupation pattern of its 3d orbital electrons, which significantly affects the catalytic performance by altering the adsorption strength of intermediates, changeing the selectivity of reaction pathways, and regulating the efficiency of electron transfer.[5] The spin state directly influences the electronic structure of the metal active center, thereby optimizing the adsorption free energy of reactant and reducing the free energy of intermediates formation (such as *COOH, OH*, etc.).[6a] For example, in the CO_2RR process, when the spin state of Ni single atom changes from a low spin (LS) state to a high spin state (HS), the d-p orbital coupling between the Ni and CO_2 strengthens, enhancing the CO_2 activation and reducing the energy barrier for formation of *COOH, thereby significantly improving the selectivity and activity for CO production.[6b] Additionally, spin state regulation can alter the adsorption configuration of reactant molecules, thereby influencing the reaction pathway. For instance, introducing heteroatoms (such as B and O) in the first-coordination shell of single atoms can break the D4h symmetry and induce spin rearrangement, which can promote the lateral adsorption of CO_2 and trigger a protonation-prioritized pathway, directly accelerating the formation of *COOH while weakening the excessive adsorption of CO, thereby avoiding catalyst poisoning and increasing CO yield.[7] The spin polarization effect can also accelerate the charge transfer process through a synergistic effect. For example, in a cooperative system of Ni nanoclusters and single atom site, the size effect of clusters can induce spin polarization at Ni single atom, promoting the dissociation of water molecules to generate *H protons, providing a rapid proton source for the protonation of CO_2, thereby significantly reducing the overpotential for CO production.[8] In recent decades, extensive strategies have been demonstrated to be highly effective in regulating the spin state of single atom active sites, such as modulating the coordination environment of

metal centers,[9] implementing strain engineering and axial functionalization,[10] harnessing the cooperative effects among neighboring atoms or clusters,[11] applying external physical field regulation,[12] and introducing carriers and co-component groups.[13] However, a comprehensive understanding of how the coordinated nitrogen species affect the spin state and the catalytic performance of SACs is still lacking.[14] Because the types of nitrogen in most reported M-N_xC catalysts are complex, such as pyridinic N, pyrrolic N, and graphitic N, and it is quite challenging to obtain highly uniform coordinated nitrogen species.[15] The primary reason is that most SACs supported on nitrogen-doped carbon (NC) carriers are synthesized via prolonged high-temperature calcination, typically exceeding 600 °C for more than two hours, during which the structure of NC support undergo reorganization and interact with metal atoms to achieve the most stable configuration, leading to the formation of hybrid nitrogen species to coordinated with metal centers. Therefore, developing an effective strategy capable of fabricating SACs with highly uniform coordinated nitrogen species is of great significance for investigating the impact of coordinated-N types on the spin state of active center.

In this work, a spin-state modulation strategy has been applied to regulate the electrocatalytic activity of single Ni atom catalysts for CO_2 reduction. Two single Ni atom catalysts with different coordinated-N species were firstly synthesized through a gas-protected joule heating process, during which the nickel metal complex precursors were rapidly carbonized at high temperature, and their coordination nitrogen configuration remained invariant. The coordination structures of two single Ni atom catalysts were confirmed to be Ni-N_4C by X-ray absorption fine structure spectra (XAFS), and the N species in these two catalysts were further deterimed to be pyrrolic-N and pyridinic-N respectively by N k-edge X-ray absorption near-edge structure spectra (XANES) and X-ray photoelectron spectroscopy (XPS) techniques. Magnetic susceptibility (M-T) measurements confirms that the Ni center in Ni-$N_{pyridinic}$-C and Ni-$N_{pyrrolic}$-C are in high spin state and low spin state, respectively. The Ni-$N_{pyridinic}$-C with high spin state can realize an excellent electrocatalytic activity and selectivity for CO_2-to-CO conversion in both H-type cell and gas diffusion flow cell. A maximum CO faradaic efficiency of 98.8% is achieved at -0.7 V and kept above 90% from -0.4 to -1.2 V (vs. RHE) in H-type cell. In gas diffusion flow cell, 99.4%, 99.3% and 99.1% CO faradaic efficiency can be obtained at industrial-level current densities ($\geq$ 250 mA cm^{-2}) in alkaline, neutral and acidic electrolytes, the CO partial current density all exceed 450 mA cm^{-2}. The applicability of the Ni-$N_{pyridinic}$-C catalyst was also demonstrated in zinc-CO_2 battery. The d-electron energy level distribution of Ni in the high-spin state is more dispersed, which strengthens the hybridization with the π^* orbital of CO_2 molecules and facilitates the adsorption and activation of CO_2, while Ni in low-spin state leads to a higher degree of degeneracy in the d-orbital energy levels and weakens the interaction with the reaction intermediates. The projected density of states (PDOS), crystal orbital Hamilton population (COHP) analysis and density functional theory (DFT) calculations further reveal that Ni-$N_{pyridinic}$-C catalyst possesses a stronger interaction with *COOH intermediate than Ni-$N_{pyrrolic}$-C, thus accelerating the electron transfer from Ni center to *COOH, leading to boosted CO_2 reduction activity.

10.1002/anie.202506845

2. Results and Discussion

2.1 Synthesis and Characterization of Single Ni Atom Catalysts with different coordinated N species

Figure 1a illustrates in detail the synthesis process of atomically dispersed Ni-N_4-C catalysts with different coordinated N species through a gas-protected flash Joule heating strategy, during which the temperature quickly increases to 2000 °C within five seconds, and the nickel metal complex precursors were rapidly carbonized at high temperature in short time. The configuration of the nickel metal complexes and the types of coordinated nitrogen have no time to change during the rapid carbonization process, leading to the fast doping of Ni and N into XC-72 carbon support. High-resolution transmission electron microscopy (HRTEM) images in Figure 1b and Figure 1e clearly reveal the irregular layer like graphitic carbon structures for as-obtained Ni-$N_{pyrrolic}$-C and Ni-$N_{pyridinic}$-C, which is inherited from the XC-72 carbon black (Figure S1). Furthermore, no clearly metal nanoparticles can be observed in the aberration-corrected high-angle annular dark-field scanning transmission electron microscopy (HAADF-STEM) images for both Ni-$N_{pyridinic}$-C and Ni-$N_{pyrrolic}$-C catalysts, and the homogeneous atomic-scale dispersed bright dots on carbon matrix are ascribed to the Ni single atoms in both catalysts (Figure 1c and Figure 1f), demonstrating the successfully synthesized single Ni atoms catalysts. Elemental mapping of Ni-$N_{pyridinic}$-C and Ni-$N_{pyrrolic}$-C in Figure 1d and Figure 1g verifies the fact that Ni single atoms and N are homogeneously distributed over the whole carbon support. Inductively coupled plasma atomic emission spectrometry (ICP-AES) measurements reveal the Ni contents in Ni-$N_{pyridinic}$-C and Ni-$N_{pyrrolic}$-C are 1.10 wt% and 1.13 wt% (Table S1), respectively. The specific surface area and pore volume of Ni-$N_{pyridinic}$-C and Ni-$N_{pyrrolic}$-C catalysts were obtained from nitrogen adsorption-desorption isotherms shown in Figure S3. As exhibited in Figure S3, both Ni-$N_{pyridinic}$-C and Ni-$N_{pyrrolic}$-C exhibit typical type III isotherms and H3 hysteresis loops in the range of $P/P^0 = 0 \sim 1.0$, revealing the existence of mesopores (Table S2). The Brunauer-Emmett-Teller (BET) surface area of Ni-$N_{pyridinic}$-C and Ni-$N_{pyrrolic}$-C are 149.98 $m^2\ g^{-1}$ and 152.26 $m^2\ g^{-1}$, respectively, indicating the highly consistent structure of these two catalysts.

Powder X-ray diffraction (PXRD) patterns in Figure 2a exhibit a broad peak at about 26 degree for both Ni-$N_{pyridinic}$-C and Ni-$N_{pyrrolic}$-C catalysts, similar with that of pure XC-72 carbon black (Figure S2), which is attributed to the graphitic carbon, and no diffraction peaks for metallic Ni can be observed, indicating no crystalline Ni species are generated in these two catalysts, which are in accordance with the HAADF-STEM results. The X ray absorption fine structure spectra (XAFS) and X-ray absorption near-edge structure (XANES) spectra at Ni K-edge were collected to explore the detailed information about the electronic structure and microchemical coordination environment of Ni active centers. As shown in Ni K-edge XANES spectra (Figure 2b), the white line

of Ni-$N_{pyridinic}$-C and Ni-$N_{pyrrolic}$-C are both located in-between that of NiO and Ni foil, very close to that of NiPc, indicating the oxidation state of monodispersed Ni in Ni-$N_{pyridinic}$-C and Ni-$N_{pyrrolic}$-C is between 0 and +2. The nearly coincident white lines of Ni-$N_{pyridinic}$-C and Ni-$N_{pyrrolic}$-C implies that the chemical states of Ni atoms in the two catalysts are essentially the same. The Fourier transformed extended X-ray absorption fine spectra (FT-EXAFS) of Ni-$N_{pyridinic}$-C, Ni-$N_{pyrrolic}$-C and NiPc in Figure 2c exhibit a prominent peak at ~1.4 Å, which is assigned to the Ni–N interaction. No peak for Ni–Ni interaction can be observed, indicating that Ni is atomically distributed in both $N_{pyridinic}$-C and Ni-$N_{pyrrolic}$-C catalysts, this result is consistent with the HAADF-STEM results. The quantitative EXAFS fitting was performed to confirm the local coordination structure of Ni atoms in $N_{pyridinic}$-C and Ni-$N_{pyrrolic}$-C catalysts. As exhibited in Figure 2d and Figure 2e, the experimental results match well with the fitting model, indicating that Ni atoms in $N_{pyridinic}$-C and Ni-$N_{pyrrolic}$-C are both coordinated with four nitrogen atoms (Figure S4 and Table S3), and the inset figure in Figure 2d and Figure 2e illustrate their probable structure, respectively. In addition, wavelet transform (WT)-EXAFS contour plots were performed in the *k*-space to clarify the backscattering atoms in the *R*-space, as shown in Figure 2g and Figure 2h, the maximum intensity of scattering path for both $N_{pyridinic}$-C and Ni-$N_{pyrrolic}$-C is at ≈ 4.6 $Å^{-1}$, which is ascribed to the Ni–N scattering path. However, the highest intensity located at ≈ 6 $Å^{-1}$ in Ni foil is attributed to the Ni–Ni scattering path (Figure S5). The above results further confirm the Ni atoms in $N_{pyridinic}$-C and Ni-$N_{pyrrolic}$-C are atomically dispersed. The nitrogen species in Ni-$N_{pyridinic}$-C and Ni-$N_{pyrrolic}$-C catalysts were investigated through N k-edge XANES and the spectra were compared in Figure 2f, in which two obvious peaks situated at 400.1 eV and 402.3 eV are corresponding to the pyridinic-N and pyrrolic-N, respectively. [16] As depicted in Figure 2f, the majority of nitrogen in Ni-$N_{pyridinic}$-C catalyst is pyridinic type, with a minor portion of pyrrolic type. While most of nitrogen in Ni-$N_{pyrrolic}$-C catalyst is pyrrolic type, with a small amount of pyridinic type. High-resolution N 1s XPS spectra of Ni-$N_{pyridinic}$-C and Ni-$N_{pyrrolic}$-C shown in Figure 2i were applied to further study the nitrogen species in these two catalysts, and the nitrogen peak in both catalysts can be divided into three peaks, i.e. 398.5 eV, 399.8 eV, and 401.5 eV, which are ascribed to the pyridinic-N, pyrrolic-N, and graphitic-N.[17] As observed in Figure 2i, the dominant nitrogen species in Ni-$N_{pyridinic}$-C and Ni-$N_{pyrrolic}$-C catalysts are pyridinic-N and pyrrolic-N, respectively, and their contents in these two catalysts respectively reach 83.4 at.% and 85.6 at.% (Table S4). These results are in good accordance with the N k-edge XANES analysis. To further explore the influence of the rapid carbonization process on nitrogen species, high-resolution N 1s XPS spectra of Ni-$N_{pyridinic}$-C and Ni-$N_{pyrrolic}$-C before and after carbonization were compared. As exhibited in Figure S6, after rapid flash joule heating process at 2000 °C, the nitrogen species in both catalysts almost remain the same with

those in uncarbonized samples, indicating the good feasibility of this materials synthesis strategy. The chemical state of Ni in Ni-$N_{pyridinic}$-C and Ni-$N_{pyrrolic}$-C catalysts were analyzed via high-resolution Ni 2p XPS spectra (Figure S8), two obvious peaks located at 855.3 eV and 873.1 eV in both Ni single atom catalysts are corresponding to the Ni $2p_{3/2}$ and Ni $2p_{1/2}$, another two clearly peaks at 861.1 eV and 879.8 eV are attributed to the satellite peaks.[18] The contents of Ni $2p_{3/2}$, Ni $2p_{1/2}$ and satellite peaks for Ni-$N_{pyridinic}$-C and Ni-$N_{pyrrolic}$-C were quantified by integrating the areas of fitted peaks and the results were shown in Table S5. The binding energy of Ni $2p_{3/2}$ and Ni $2p_{3/2}$ in both Ni-$N_{pyridinic}$-C and Ni-$N_{pyrrolic}$-C catalysts shift towards positive direction when compared with XPS spectra of Ni metal (Ni $2p_{3/2}$ 852.4 eV, Ni $2p_{1/2}$ 869.6 eV), indicating a positive oxidation state of Ni in Ni-$N_{pyridinic}$-C and Ni-$N_{pyrrolic}$-C catalysts. The coexistence of Ni $2p_{3/2}$, Ni $2p_{1/2}$ and related satellite peaks in Ni-$N_{pyridinic}$-C and Ni-$N_{pyrrolic}$-C indicates the mixed-valence state of Ni in Ni-$N_{pyridinic}$-C and Ni-$N_{pyrrolic}$-C. These results are consistent with the Ni K-edge XANES results in Figure 2b. From the above analysis, we can conclude that two Ni single atom catalysts with Ni-N4 coordinated structure are successfully synthesized, and the most significant disparity between two Ni single atom catalysts is the type of coordinated nitrogen.

2.2 Electrochemical CO_2 Reduction Performance of Ni-N-C in H-type cell and Flow-cell.

The electrocatalytic CO_2 reduction performance of the as-synthesized Ni-$N_{pyridinic}$-C and Ni-$N_{pyrrolic}$-C catalysts was first evaluated in standard three-electrode H-type cell with CO_2/Ar-saturated 0.5 M $KHCO_3$ solution as electrolyte. Linear sweep voltammetry (LSV) curves in Figure 3a exhibit that both Ni-$N_{pyridinic}$-C and Ni-$N_{pyrrolic}$-C achieve the higher current density in CO_2 saturated electrolyte than that in Ar saturated electrolyte, indicating the electrocatalytic activity of Ni-$N_{pyridinic}$-C and Ni-$N_{pyrrolic}$-C for CO_2 reduction. In addition, Ni-$N_{pyridinic}$-C exhibits a larger current density than Ni-$N_{pyrrolic}$-C in the entire testing voltage range. The gaseous and liquid products were detected separately using GC and ^{1}H NMR spectrum after constant potential electrolysis. H_2 and CO are the only gaseous products (Figure S9, S11 and S12) and no liquid products were detected (Figure S10). As can be seen from Figure 3b, Ni-$N_{pyridinic}$-C exhibits higher faradaic efficiency for CO than Ni-$N_{pyrrolic}$-C with the whole potential range and attains the maximum CO faradaic efficiency 98.8% at -0.7 V *vs*. RHE, which is significantly higher than that of Ni-$N_{pyrrolic}$-C (76.4%). From -0.4 to -1.2 V *vs*. RHE, the CO faradaic efficiency of Ni-$N_{pyridinic}$-C maintains above 90%, demonstrating the high activity and product selectivity of Ni-$N_{pyridinic}$-C. To eliminate the influence of precursors on the electrocatalytic performance, the electrochemical performance of Ni-$N_{pyrrolic}$ and Ni-$N_{pyridinic}$ precursor before calcination for CO_2 reduction were investigated, their LSV curves and CO faradaic efficiency were further compared with those of Ni-$N_{pyrrolic}$-C and Ni-$N_{pyridinic}$-C in Figure S13. The current densities and CO

faradaic efficiency of Ni-$N_{pyrrolic}$ precursor and Ni-$N_{pyridinic}$ precursor are significantly lower than those of the Ni-$N_{pyrrolic}$-C and Ni-$N_{pyridinic}$-C in the whole potential range, indicating that the outstanding electrocatalytic activity of Ni-$N_{pyridinic}$-C does not originate from the precursor. Subsequently, the electrocatalytic activities of nickel-free carriers ($N_{pyridinic}$-C and $N_{pyrrolic}$-C) for CO_2 reduction were studied, and the CO_2 electroreduction performance exhibited by the two nickel-free carriers can be disregarded (Figure S14), further confirming that the superior catalytic performance of Ni-$N_{pyridinic}$-C does not come from the $N_{pyridinic}$-C carrier. The CO partial current density (Figure 3c) and turn oner frequency (TOF) per nickel site (Figure 3d) achieved on Ni-$N_{pyridinic}$-C is significantly higher than those on Ni-$N_{pyrrolic}$-C at same potential, also confirming the excellent catalytic performance of Ni-$N_{pyridinic}$-C for CO_2 reduction. Figure 3e displays the durability measurement of Ni-$N_{pyridinic}$-C in H-type cell, in which it can be observed that the current density and CO faradaic efficiency of Ni-$N_{pyridinic}$-C almost keep constant with negligible attenuation during 80 hours electrolysis, revealing the outstanding stability of Ni-$N_{pyridinic}$-C. After durability measurements, no obviously changes were observed in the SEM images (Figure S19), XRD patterns (Figure S18), and XPS spectra (Figure S22) of Ni-$N_{pyridinic}$-C and Ni-$N_{pyrrolic}$-C, and Ni atoms still homogeneously disperse on the whole structure of Ni-$N_{pyridinic}$-C (Figure S20-S21), further demonstrating the excellent stability of Ni-$N_{pyridinic}$-C and Ni-$N_{pyrrolic}$-C. Furthermore, the electrolyte after durability measurement was analyzed by ICP-OES and no Ni species was detected. The catalytic performance of Ni-$N_{pyridinic}$-C in H-type cell was compared with the previously reported Ni-based electrocatalysts in Table S6, in which the CO faradaic efficiency and durability of Ni-$N_{pyridinic}$-C surpass majority of the reported Ni-based electrocatalysts, accompanied with a significantly larger current density. For the purpose of exploring the origin of the higher catalytic activity of Ni-$N_{pyridinic}$-C than Ni-$N_{pyrrolic}$-C, electrochemical active surface areas (ECSA) of Ni-$N_{pyridinic}$-C and Ni-$N_{pyrrolic}$-C were acquired from the double-layer capacitances (C_{dl}) with cyclic voltammetry measurement in no-faradaic potential range. As illustrated in Figure S15, Ni-$N_{pyridinic}$-C (14.12 mF cm^{-2}) and Ni-$N_{pyrrolic}$-C (13.88 mF cm^{-2}) possess the nearly identical capacitances, which are consistent with the BET surface areas shown in Figure S3 and Table S2, indicating that the quantity of exposed reactive sites almost the same, and the ECSA and specific surface area of Ni-$N_{pyridinic}$-C and Ni-$N_{pyrrolic}$-C are not the decisive factors for their catalytic performance for CO_2 reduction. Subsequently, Tafel plots were applied to investigate the CO_2 reduction reaction kinetics, as illustrated in Figure S16, Ni-$N_{pyridinic}$-C exhibits an expected smaller Tafel slope (174.06 mV dec^{-1}) than Ni-$N_{pyridinic}$-C (236.41 mV dec^{-1}), suggesting the superior CO_2 reduction reaction kinetics of Ni-$N_{pyridinic}$-C. The electrochemical impedance spectroscopy (EIS) of Ni-$N_{pyridinic}$-C and Ni-$N_{pyrrolic}$-C during CO_2 reduction were further measured to investigate the reaction kinetics. As shown in Figure S17, Ni-

$N_{pyridinic}$-C exhibits an obvious smaller semidiameter than Ni-$N_{pyrrolic}$-C, indicating a faster electron transfer speed and reaction kinetics of Ni-$N_{pyridinic}$-C for CO_2 electroreduction. From the abovementioned analysis, we can conclude that the dissimilarity in the catalytic activities of Ni-$N_{pyridinic}$-C and Ni-$N_{pyrrolic}$-C is mainly attributed to variance in the types of coordinated nitrogen, the pyridinic-N coordinated Ni active center has the superior intrinsic activity and product selectivity than the pyrrolic-N coordinated Ni atoms.

The practical applicability of Ni-$N_{pyridinic}$-C for CO_2 reduction under industrial-level current density (> 300 mA cm^{-2}) was evaluated in gas-diffusion flow-cell, and the structure is detailed illustrated in Figure S23, in which gaseous CO_2 directly contact with the catalyst and then be reduced at the solid-liquid-gas triple-phase interface. As listed in Figure 3f, Ni-$N_{pyridinic}$-C can achieve the industrial-level CO partial current densities in all alkaline, neutral and acidic electrolytes, and the maximum current densities are 494.4 mA cm^{-2}, 459.1 mA cm^{-2} and 479.2 mA cm^{-2}, respectively, far surpassing industrial-level current density requirements for industrial application. The maximum CO Faradaic efficiency in alkaline electrolyte (KOH) attains 99.4% at current density of -250 mA cm^{-2}, and maintains above 98.1% in a wide current density range of -50 – -500 mA cm^{-2} (Figure 3g). In neutral electrolyte ($KHCO_3$), Ni-$N_{pyridinic}$-C achieves the maximum CO Faradaic efficiency of 99.4% at -300 mA cm^{-2}, retaining above 98.1% from -50 mA cm^{-2} to -350 mA cm^{-2}, and then gradually descends to 91.8% at -500 mA cm^{-2}. Remarkably, the CO Faradaic efficiency can still reach 99.1% in acidic electrolyte at current density of -250 mA cm^{-2} and keeps above 95.8% in the whole testing current density range. Furthermore, the durability of Ni-$N_{pyridinic}$-C in gas-diffusion flow-cell with alkaline, neutral and acidic electrolytes were also investigated. As shown in Figure 3h, the CO Faradaic efficiency of Ni-$N_{pyridinic}$-C can still maintain above 94.7% 93.1% and 99.4% at a constant current density of -100 mA cm^{-2} for 45 hours. In addition, after 24 hours measurements at -300 mA cm^{-2}, the CO Faradaic efficiency of Ni-$N_{pyridinic}$-C can remain above 94.01%, 96% and 95.03% in alkaline, neutral, and acidic electrolyte, respectively (Figure S24). These durability measurements demonstrate the outstanding stability of Ni-$N_{pyridinic}$-C at high current density in wide pH range. The performance of Ni-$N_{pyridinic}$-C in gas-diffusion flow-cell with alkaline, neutral and acidic electrolytes were compared with the previously reported electrocatalysts in Table S7, and Ni-$N_{pyridinic}$-C exceeds most of the reported catalysts. The exceptional catalytic activity and durability of Ni-$N_{pyridinic}$-C in both H-type cell and gas-diffusion flow-cell at wide pH range electrolyte foretell the prospect for industrial application.

2.3 Zinc-CO_2 battery

The primary aqueous zinc-CO_2 battery based Ni-$N_{pyridinic}$-C was constructed and further used to evaluated the practical applicability of Ni-$N_{pyridinic}$-C for CO_2 reduction.

Figure 4a exhibits the detailed structure of zinc-CO_2 battery, in which carbon paper loaded with the Ni-$N_{pyridinic}$-C serves as cathode and zinc foil works as anode, and the catholyte ($KHCO_3$) and anolyte (KOH) is separated by an bipolar membrane. The discharge and charge voltages under different current densities are exhibited in Figure 4b, in which an obvious rechargeable behavior of the assembled zinc-CO_2 battery can be observed. The zinc-CO_2 battery could deliver a maximum power density of 1.89 mW cm^{-2} at a discharge current density of 4.0 mA cm^{-2} during discharge (Figure 4b). The CO_2 reduction products in zinc-CO_2 battery during the discharge process were detected, and the Faradaic efficiency was compared in Figure 4c. As shown in Figure 4c, Ni-$N_{pyridinic}$-C equipped in the zinc-CO_2 battery displays an excellent CO selectivity within the discharge process with a maximum CO Faradaic efficiency of 96.0% at 7.0 mA cm^{-2}, meanwhile, the CO Faradaic efficiency can maintain above 92.1% in a wide range of discharge current density (2.0 ~ 7.0 mA cm^{-2}). At the constant discharge current density of 1.0 mA cm^{-2}, the discharge voltage maintains at 0.42 V, and then gradually decreases with the increasing of the discharge current density from 1.0 mA cm^{-2} to 7.0 mA cm^{-2}. The discharge voltage can retain stable at different discharge current densities. The galvanostatic charge-discharge cycling at discharge current density of 1 mA cm^{-2} and 2 mA cm^{-2} in Figure 4e reveal the high stability of Ni-$N_{pyridinic}$-C during battery cycling. No obvious voltage decay can be observed during 200 charge-discharge cycles at 1 mA cm^{-2} and 180 charge-discharge cycles at 2 mA cm^{-2}, manifesting the outstanding stability of the assembled zinc-CO_2 battery. XRD, XPS and HRTEM were further applied to investigate the stability of Ni-$N_{pyridinic}$-C in Zn-CO_2 battery. After charge-discharge cycles, no obviously changes can be observed in the XRD patterns (Figure S25), XPS spectra (Figure S25) and HRTEM images (Figure S26) of Ni-$N_{pyridinic}$-C, and Ni atoms still homogeneously disperse on the whole structure of Ni-$N_{pyridinic}$-C (Figure S26), confirming the superior stability of Ni-$N_{pyridinic}$-C. The maximum power density, FE_{CO} and durability of Ni-$N_{pyridinic}$-C in Zn-CO_2 battery were further compared with the previously reported electrocatalysts in Table S8, and Ni-$N_{pyridinic}$-C exhibited the superior electrochemical performance in Zn-CO_2 battery than most of the reported single atom electrocatalysts. The abovementioned results demonstrate the promising applicability of Ni-$N_{pyridinic}$-C in zinc-CO_2 battery.

2.4 Investigation of Catalytic Mechanism

To clarify the different CO_2 reduction activity as well as the reduction mechanism over Ni-$N_{pyridinic}$-C and Ni-$N_{pyrrolic}$-C catalysts, in-situ attenuated total reflection infrared spectroscopy (ATR-IR) measurements at different potentials were conducted to probe the reaction intermediates. Figure 5a and 5b exhibit the in-situ ATR-IR spectra of CO_2 reduction on Ni-$N_{pyridinic}$-C and Ni-$N_{pyrrolic}$-C respectively, in which *COOH (1407 cm^{-1}), H_2O (1641 cm^{-1}), CO (1915 cm^{-1}) and CO_2 (2360 cm^{-1}) can be clearly observed in both spectra.[19] As the reaction potential increases from -0.2 V to -1.2 V,

the absorbance of CO_2 decreases, indicating the continuously consumed CO_2 during the reaction. The peak intensities of *COOH key intermediate and adsorbed H_2O both gradually increase for Ni-$N_{pyridinic}$-C and Ni-$N_{pyrrolic}$-C as the overpotential increased, demonstrating that the *COOH intermediate formation is the rate-determining step for CO_2 reduction, and the H_2O is the proton source for CO_2 reduction. The gradually increased CO intensity at higher overpotential indicates the accumulation of the generated CO at high overpotential. The peak intensities of *COOH and CO on Ni-$N_{pyridinic}$-C are significantly larger than those of on Ni-$N_{pyrrolic}$-C, indicating the superior catalytic activity of Ni-$N_{pyridinic}$-C for CO_2 reduction.

The CO_2 adsorption capacities of Ni-$N_{pyridinic}$-C and Ni-$N_{pyrrolic}$-C were evaluated by CO_2 adsorption isotherms. As displayed in Figure S27, Ni-$N_{pyridinic}$-C and Ni-$N_{pyrrolic}$-C exhibit the similar adsorption curves for CO_2, and the maximum CO_2 adsorption capacities of Ni-$N_{pyridinic}$-C and Ni-$N_{pyrrolic}$-C are 2.37 $cm^3\ g^{-1}$ and 2.41 $cm^3\ g^{-1}$ at $P/P^0 = 1.0$, indicating the similar CO_2 adsorption capacities of Ni active sites in both electrocatalysts. This result demonstrates that the CO_2 adsorption ability is not the key determinant for the catalytic performance of Ni-$N_{pyridinic}$-C and Ni-$N_{pyrrolic}$-C for CO_2 reduction. In order to gain deep insights into the electron spin configuration effect of Ni-$N_{pyridinic}$-C and Ni-$N_{pyrrolic}$-C on their electrocatalytic activities for CO_2 reduction, the electron paramagnetic resonance (EPR) spectroscopy of Ni-$N_{pyridinic}$-C and Ni-$N_{pyrrolic}$-C were conducted. As exhibited in Figure S28, Ni-$N_{pyridinic}$-C displays an obvious peak at ~ 3000 Gauss with a g-factor of ~2, while the peak density of Ni-$N_{pyrrolic}$-C is significantly weaker than that of Ni-$N_{pyridinic}$-C, indicating a higher abundance of unpaired electrons in the Ni 3d orbitals of Ni-$N_{pyridinic}$-C than Ni-$N_{pyrrolic}$-C. Subsequently, the unpaired 3d electrons and spin states of Ni active center in Ni-$N_{pyridinic}$-C and Ni-$N_{pyrrolic}$-C were further analyzed by Ni K-edge XANES spectra and Fourier transform EXAFS spectra. The white line position at ~ 8334 eV represents the quadrupole-allowed transition from 1s to 3d, and at ~ 8340 eV represents the 1s to 4pz transition.[20] As observed in enlarged XANES spectra of Ni-$N_{pyridinic}$-C and Ni-$N_{pyrrolic}$-C in Figure S29, Ni-$N_{pyridinic}$-C exhibits an increased intensity at 8334 eV than Ni-$N_{pyrrolic}$-C, and this is ascribed to the hybridization of the 3d and 4p orbitals, which leads to the spin allowed transitions from 1s to 4p.[20] At 8340 eV, Ni-$N_{pyridinic}$-C also displays an increased intensity than Ni-$N_{pyrrolic}$-C, indicating the higher amounts of unpaired 3d electrons in Ni-$N_{pyridinic}$-C, [21] and this is consistent with the result of EPR. The enlarged Fourier transform EXAFS spectra of Ni-$N_{pyridinic}$-C and Ni-$N_{pyrrolic}$-C were further compared, and the peak position of Ni-$N_{pyridinic}$-C had a slightly shift towards the direction of longer Ni-N distance than Ni-$N_{pyrrolic}$-C, indicating a slightly longer Ni-N distance in Ni-$N_{pyridinic}$-C than that in Ni-$N_{pyrrolic}$-C and a high-spin state of Ni-N species in Ni-$N_{pyridinic}$-C.[22] In addition, the spin state of Ni-$N_{pyridinic}$-C and Ni-$N_{pyrrolic}$-C were confirmed by the magnetic susceptibility (M-T) measurements (Figure 5c). According

10.1002/anie.202506845

to the Curie-Weiss law,[23] the effective magnetic moments (μ_{eff}) of Ni-$N_{pyridinic}$-C and Ni-$N_{pyrrolic}$-C are determined to be 2.83 μB and 1.05 μB respectively, and the unpaired electrons in 3d orbital of Ni center in Ni-$N_{pyridinic}$-C is verified to be 2, while in Ni-$N_{pyrrolic}$-C is confirmed to be 0, indicating that the Ni center in Ni-$N_{pyridinic}$-C and Ni-$N_{pyrrolic}$-C is in high spin state and low spin state, respectively. Calculated projected density of states (PDOS) of Ni^{2+} in Ni-$N_{pyridinic}$-C and Ni-$N_{pyrrolic}$-C were further applied to investigate the spin-state of Ni center. As displayed in Figure S30, the Ni active center in Ni-$N_{pyridinic}$-C shows a $d_{xy}(4)$, $d_{xz,yz}(2)$, $d_z^2(1)$, $d_{x^2-y^2}(1)$ configuration with a high-spin state, while in Ni-$N_{pyrrolic}$-C is low-spin state with a $d_{xy}(4)$, $d_{xz,yz}(2)$, $d_z^2(2)$, $d_{x^2-y^2}(0)$ configuration. This is in good agreement with the M-T results.

The distinct spin states of the 3d orbitals on the Ni active center is ascribed to the different coordinated N species, which can significantly affect the adsorption/desorption behavior of the CO_2 and reaction intermediates (*COOH and *CO) (Figure S31) along the z-axis direction during the CO_2 reduction process, thereby leading to the obvious differences in catalytic activities. Figure S32 illustrates the adsorption energy of CO_2 on Ni centers in Ni-$N_{pyridinic}$-C and Ni-$N_{pyrrolic}$-C, respectively, an obviously higher adsorption energy can be observed for Ni-$N_{pyridinic}$-C (-0.136 eV) than Ni-$N_{pyrrolic}$-C (-0.122 eV), indicating the stronger adsorption ability and more activation probability of Ni-$N_{pyridinic}$-C for CO_2. To elucidate the influence of electron spin states on CO_2 reduction kinetics, the projected density of states (PDOS) of Ni-$N_{pyridinic}$-C and Ni-$N_{pyrrolic}$-C was subsequently computed. As displayed in Figure 5f, the overlapping between Ni-3d orbital and *COOH-2p orbital over Ni-$N_{pyridinic}$-C is more obvious than that over Ni-$N_{pyrrolic}$-C, indicating a stronger interaction. Furthermore, the closer d band center of Ni-$N_{pyridinic}$-C to Femi level implies an enhanced reaction kinetics. To further clarify the spin state effect on catalytic activity, the spin density diagrams of Ni center with *COOH intermediate were visualized in Figure 5d. The partially occupied d_Z^2 orbital in high spin state of Ni-$N_{pyridinic}$-C can form a $\sigma*$ orbital with *COOH (Figure 5d), and promote the interaction between *COOH and Ni center, therefore boosting the reaction kinetics of *COOH formation and further reduction. Crystal orbital Hamilton population (COHP) analysis of Ni-$N_{pyridinic}$-C and Ni-$N_{pyrrolic}$-C bonding and anti-bonding state with *COOH were further conducted to investigate the nature of Ni-*COOH interaction (Figure 5g). The ICOHP value of Ni-$N_{pyridinic}$-COOH is determined to be -1.391 eV, obviously larger than -1.149 eV of Ni-$N_{pyrrolic}$-COOH, suggesting stronger Ni-*COOH interaction over Ni-$N_{pyridinic}$-C. Subsequently, the charge density difference and Bader charge (Figure 5e) were conducted to investigate the electron transfer behaviors. Compared to Ni-$N_{pyrrolic}$-C (0.10 e), Ni-$N_{pyridinic}$-C can endow more charge (0.30 e) to the adsorbed *COOH, therefore facilitating the *COOH interaction and activation.

To further investigate the origin of high catalytic activity of Ni-$N_{pyridinic}$-C, first-principles density functional theory (DFT) calculations were conducted (details are shown in theoretical and computational methods), during which the configuration of Ni sites coordinated with four pyrrolic-N and four pyridinic-N were applied as calculation models. According to the above mentioned in-situ ATR-IR analysis, *COOH and *CO are main intermediates for CO_2 reduction to CO. The Gibbs free energy change (Δ_G) diagrams of Ni-$N_{pyridinic}$-C and Ni-$N_{pyrrolic}$-C for CO_2 reduction to CO indicate the formation of *COOH is the rate-determining step for both catalysts (Figure 5h). As shown in Figure 5h, the four pyridinic-N coordinated Ni center exhibits a lower free energy change (1.57 eV) for *COOH formation than that on four pyrrolic-N coordinated Ni center (1.94 eV), indicating an easier formation of *COOH on Ni-$N_{pyridinic}$-C than on Ni-$N_{pyrrolic}$-C, thus leading to the higher activity of Ni-$N_{pyridinic}$-C. The Gibbs free energy change (Δ_G) diagrams (Figure S32a) of Ni-$N_{pyridinic}$-C and Ni-$N_{pyrrolic}$-C for hydrogen evolution reveal that the formation energy of *H on Ni-$N_{pyrrolic}$-C (0.76 eV) is significantly lower than that on Ni-$N_{pyridinic}$-C (1.55 eV), demonstrating a faster reaction kinetics of Ni-$N_{pyrrolic}$-C for hydrogen formation. To evaluate the selectivity of CO_2 reduction towards hydrogen evolution reaction, the limiting potentials difference between CO_2 to CO conversion and hydrogen evolution reaction ($U_L(CO_2)$-$U_L(H_2)$) was calculated. As exhibited in Figure S32b, Ni-$N_{pyridinic}$-C displays an obvious smaller value than Ni-$N_{pyrrolic}$-C, which indicates a higher CO_2 to CO selectivity of Ni-$N_{pyridinic}$-C. From above mentioned analysis, we can summarize that the disparity in catalytic activity of Ni-$N_{pyridinic}$-C and Ni-$N_{pyrrolic}$-C towards CO_2 reduction is mainly ascribed to the distinct types of coordinated nitrogen in Ni-N active centers. The high spin state of Ni in Ni-$N_{pyridinic}$-C active center can effectively strengthen the interaction between Ni center and *COOH intermediate and facilitate the electron transfer from Ni to *COOH by a high filling state in anti-bond orbitals, thereby activating the Ni single atomic site to boost the CO_2 reduction.

3. Conclusion

In summary, we have proposed a spin state modulating strategy to regualte the electrochemical performance of Ni single atom catalyst for CO_2 reduction. Two Ni-N_4C single atom catalysts with different coordinated N species were successfully synthesized through a gas-protected Joule heating strategy and the coordinated-N species in these two catalysts were confirmed to be pyridinic-N and pyrrolic-N, respectively. M-T measurements demonstrated that the Ni in Ni-$N_{pyridinic}$-C is in high spin state, while in Ni-$N_{pyrrolic}$-C is in low spin state. The Ni-$N_{pyridinic}$-C catalyst with high spin state could achieve an excellent electrocatalytic activity and CO Faradaic efficiency for CO_2 reduction. In H-type cell, the maximum FE_{CO} of Ni-$N_{pyridinic}$-C reaches 98.8% at -0.7 V and keeps above 90% from -0.4 to -1.2 V, which are significantly larger than those of Ni-$N_{pyrrolic}$-C. While in gas-diffusion flow cell, the CO

partial current density in alkaline, acid and neutral electrolyte all exceed 450 mA/cm^2, with the over 90% CO Faradaic efficiency. The applicability of the Ni-$N_{pyridinic}$-C catalyst was also demonstrated in zinc-CO_2 battery. PDOS, COHP and DFT calculations demonstrate that Ni-$N_{pyridinic}$-C possesses a possesses a high spin state Ni, which effectively strengthen the interaction between Ni 3d-orbital and C 2p-orbital of *COOH, accelerate the electron transfer from Ni center to *COOH, leading to the boosted CO_2 reduction activity. The spin state manipulation strategy proposed in this work provides a new avenue to rationally design highly efficient single atom catalysts for CO_2 reduction.

Acknowledgements

This work was supported by the National Natural Science Foundation of China (No. 92061201, 21825106, 22271261), Thousand Talents (Zhongyuan Scholars) Program of Henan Province (234000510007), and Postdoctoral Science Foundation of China (2022T150554). The DFT calculation is supported by Supercomputer Center in Zhengzhou University (Zhengzhou).

Conflict of Interest

The authors declare no conflict of interest.

Reference

[1] a) C. Hu, X. Hong, M. Liu, K. Shen, L. Chen, Y. Li, *Adv. Mater.* **2024**, *36*, 2409531; b)C. Hu, W. Yao, X. Yang, K. Shen, L. Chen, Y. Li, *Adv. Sci.* **2023**, *11*, 2306095; c) J. Y. T. Kim, P. Zhu, F.-Y. Chen, Z.-Y. Wu, D. A. Cullen, H. Wang, *Nat. Catal.* **2022**, *5*, 288–299; d)Y. Cheng, Q. Li, M. I. B. Salaman, C. Wei, Q. Wang, X. Ma, B. Liu, A. B. Wong, *J. Am. Chem. Soc.* **2025**, *147*, 12438–12448.

[2] a) Z. Ma, B. Wang, X. Yang, C. Ma, W. Wang, C. Chen, F. Liang, N. Zhang, H. Zhang, Y. Chu, Z. Zhuang, H. Xu, Y. Wang, J. Liu, *J. Am. Chem. Soc.* **2024**, *146*, 29140–29149; b)M. C. O. Monteiro, F. Dattila, B. Hagedoorn, R. García-Muelas, N. López, M. T. M. Koper, *Nat. Catal.* **2021**, *4*, 654–662; c)X. Liu, M. T. M. Koper, *J. Am. Chem. Soc.* **2024**, *146*, 5242–5251; d)Y. Li, J. Li, W. Ai, J. Chen, T. Lu, X. Liao, W. Wang, R. Huang, Z. Chen, J. Wu, F. Cheng, H. Wang, *Angew. Chem. Int. Ed.* **2024**, *63*, e202407772.

[3] a) M. Liu, Y. Yang, W. Zhang, G. Wu, Q. Huang, J. Wen, D. Wang, *Angew. Chem. Int. Ed.* **2025**; b) J. Song, D. He, X. Ma, P. Liu, W. Guo, R. Sun, F. Li, Z. Zhong, H. Zhou, J. Tang, J. Xu, T. Wu, L. Hu, Y. Wu, *J. Am. Chem. Soc.* **2025**; c)Z. Zhang, X. Huang, Z. Chen, J. Zhu, B. Endrődi, C. Janáky, D. Deng, *Angew. Chem. Int. Ed.* **2023**, *62*, e202302789.

[4] a) W. Sun, S. Liu, H. Sun, H. Hu, J. Li, L. Wei, Z. Tian, Q. Chen, J. Su, L. Chen, *Adv. Energy Mater.* **2025**, 2500283; b) Y. Zeng, J. Zhao, S. Wang, X. Ren, Y. Tan, Y.-R. Lu, S. Xi, J. Wang, F. Jaouen, X. Li, Y. Huang, T. Zhang, B. Liu, *J. Am. Chem. Soc.* **2023**, *145*, 15600–15610; c) J. Chen, C. Hu, Y. Liu, Y. Wei, K. Shen, L. Chen, Y. Li, *Angew. Chem. Int. Ed.* **2024**, *64*, e202422775; d) J.-C. Liu,

F. Luo, J. Li, *J. Am. Chem. Soc.* **2023**, *145*, 25264–25273; e) Y. Zhou, Q. Zhou, H. Liu, W. Xu, Z. Wang, S. Qiao, H. Ding, D. Chen, J. Zhu, Z. Qi, X. Wu, Q. He, L. Song, *Nat. Commun.* **2023**, *17*, 3776.

[5] a)Y. Zhang, Q. Wu, J. Z. Y. Seow, Y. Jia, X. Ren, Z. J. Xu, *Chem. Soc. Rev.* **2024**, *53*, 8123-8136; b)J. Qian, T. Wang, Z. Zhang, Y. Liu, J. Li, D. Gao, *Nano Energy.* **2020**, *74*, 104948; c)P. Saha, S. Amanullah, A. Dey, *Acc. Chem. Res.* **2022**, *55*, 134–144.

[6] a) J. Song, D. He, X. Ma, P. Liu, W. Guo, R. Sun, F. Li, Z. Zhong, H. Zhou, J. Tang, J. Xu, T. Wu, L. Hu, Y. Wu, *J. Am. Chem. Soc.* **2025**, https://doi.org/10.1021/jacs.5c00858; b) K. Miao, J. Qin, S. Lai, M. Luo, A. Kuchkaev, D. Yakhvarov, X. Kang, *Adv. Funct. Mater.* **2024**, 2419989.

[7] a) J. Liu, B. Han, X. Liu, S. Liang, Y. Fu, J. He, L.-H. Chung,Y. Lin, Y. Wei, S. Wang, T. Ma, Z. Yang, *Angew. Chem. Int. Ed.* **2025**, *64*, e202417435; b) X. Gu, Y. Jiao, B. Wei, T. Xu, P. Zhai, Y. Wei, J. Zuo, W. Liu, Q. Chen, Z. Yang, F. Zhao, X. Wang, L. Wang, Y. Gong, *Mater. Today* **2022**, *54*, 63-71. c) Y. Zang, Y. Liu, R. Lu, Q. Yang, B. Wang, M. Zhang, Y. Mao, Z. Wang, Y. Lum, *Adv. Mater.* **2025**, 2417034.

[8] a) K. Miao, J Qin, J. Yang, X. Kang, *Adv. Funct. Mater.* **2024**, *34*, 2316824; b) G. Luo, M. Song, Q. Zhang, L. An, T. Shen, S. Wang, H. Hu, X. Huang, D. Wang, *Nano-Micro Lett.* **2024**, *16*, 241.

[9] a)J. Zhang, F. Li, W. Liu, Q. Wang, X. Li, S.-F. Hung, H. Yang, B. Liu, *Angew. Chem. Int. Ed.* **2024**, *63*, e202412245; b)Y. Li, H. Sun, L. Ren, K. Sun, L. Gao, X. Jin, Q. Xu, W. Liu, X. Sun, *Angew. Chem. Int. Ed.* **2024**, *63*, e202405334.

[10] a)H. Zhang, X. Jin, J.-M. Lee, X. Wang, *ACS Nano.* **2022**, *16*, 17572–17592;

[11] L. Zhang, X. Ren, X. Zhao, Y. Zhu, R. Pang, P. Cui, Y. Jia, S. Li, Z. Zhang, *Nano Lett.* **2022**, *22*, 3744–3750.

[12] C. Y. Zhang, C. Zhang, G. W. Sun, J. L. Pan, L. Gong, G. Z. Sun, J. J. Biendicho, L. Balcells, X. L. Fan, J. R. Morante, J. Y. Zhou, A. Cabot, *Angew. Chem. Int. Ed.* **2022**, *61*, e202211570.

[13] C.-C. Lin, T.-R. Liu, S.-R. Lin, K. M. Boopathi, C.-H. Chiang, W.-Y. Tzeng, W.-H. C. Chien, H.-S. Hsu, C.-W. Luo, H.-Y. Tsai, H.-A. Chen, P.-C. Kuo, J. Shiue, J.-W. Chiou, W.-F. Pong, C.-C. Chen, C.-W. Chen, *J. Am. Chem. Soc.* **2022**, *144*, 15718–15726.

[14] K. Kim, G. Kim, T. Jeong, W. Lee, Y. Yang, B.-H. Kim, B. Kim, B. Lee, J. Kang, M. Kim, *J. Am. Chem. Soc.* **2024**, *146*, 34033–34042.

[15] a) Q. Wang, T. Luo, X. Cao, Y. Gong, Y. Liu, Y. Xiao, H. Li, F. Gröbmeyer, Y.-R. Lu, T.-S. Chan, C. Ma, K. Liu, J. Fu, S. Zhang, C. Liu, Z. Lin, L. Chai, E. Cortes, M. Liu, *Nat. Commun.* **2025**, *16*, 1985; b)S. Wei, J. Zhu, X. Chen, R. Yang, K. Gu, L. Li, C.-Y. Chiang, L. Mai, S. Chen, *Nat. Commun.* **2025**, *16*, 1652; c)C. Hu, Y. Zhang, A. Hu, Y. Wang, X. Wei, K. Shen, L. Chen, Y. Li, *Adv. Mater.* **2023**, *35*, 2209298.

[16] a) H. Su, W. Zhou, W. Zhou, Y. Li, L. Zheng, H. Zhang, M. Liu, X. Zhang, X. Sun, Y. Xu, F. Hu, J. Zhang, T. Hu, Q. Liu, S. Wei, *Nat. Commun.* **2021**, *12*,

6118; b) Z. Sun, C. Li, Z. Wei, F. Zhang, Z. Deng, K. Zhou, Y. Wang, J. Guo, J. Yang, Z. Xiang, P. Ma, H. Zhai, S. Li, W. Chen, *Adv. Mater.* **2024**, *36*, 2404665.

[17] a) Z. Jiang, Z. H. Lyu, X. Z. Liu, J. Fu, L. Zhang, Z. C. Yao, L. R. Zheng, D. Su, Y. J. Fan, T. Tang, J. S. Hu, *Adv. Funct. Mater.* **2024**, 2401927; b) J. R. Huang, X. F. Qiu, Z. H. Zhao, H. L. Zhu, Y. C. Liu, W. Shi, P. Q. Liao, X. M. Chen, *Angew. Chem.* **2022**, *134*, e202210985; c) L. Yingxi, X. Chenfeng, Z. Zhaozhao, W. Junjie, N. Huiting, G. Shuning, L. Zhao, Y. Na, C. Jun Song, W. Rui, X. Bao Yu, *Angew. Chem. Int. Ed.* **2024**, e202414569.

[18] a) Y. Li, S. L. Zhang, W. Cheng, Y. Chen, D. Luan, S. Gao, X. W. D. Lou, *Adv. Mater.* **2021**, *34*, 2105204; b) C. Sayantan, C. Rupak, R. Samim, P. Snigdha, T. Ranjit, B. Rajaram, B. Asim, *Adv. Energy Mater.* **2024**, 2403809; c) L. Yinghui, R. Li, Y. Yingying, Z. Yingyan, X. Hao, L. Zhao, L. Zi, d. Xiaohan, T. Yuhan, C. Shusheng, L. Xi, Y. Chongnan, Z. Andreas, Z. Jianxin, *Adv. Funct. Mater.* **2024**, 2417915.

[19] a) C. Wang, Z. Lv, Y. Liu, R. Liu, C. Sun, J. Wang, L. Li, X. Liu, X. Feng, W. Yang, B. Wang, *Angew. Chem. Int. Ed.* **2024**, *63*, e202404015; b) R. Boppella, M. Austeria P, Y. Kim, E. Kim, I. Song, Y. Eom, D. P. Kumar, M. Balamurugan, E. Sim, D. H. Kim, T. K. Kim, *Adv. Funct. Mater.* **2022**, *32*, 2202351; c) J. Yan, J. Ni, H. Sun, C. Su, B. Liu, *Chin. J. Catal.* **2024**, *62*, 32-52; d) Z. Tao, A. J. Pearce, J. M. Mayer, H. Wang, *J. Am. Chem. Soc.* **2022**, *144*, 8641–8648.

[20] a) J. Hahn, M. Co, D. Spira, K. Hodgson, E. Solomon, *Biochem. Biophys. Res. Commun.* **1983**,*112*, 737-745; b) J. Hahn, R. Scott, K. Hodgson, S. Doniach, E. Solomon, *Chem. Phys. Lett.* **1982**, *88*, 595-598; c) X. Wang, Y. Fu, D. Tranca, K. Jiang, J. Zhu, J. Zhang, S. Han, C. Ke, C. Lu, X. Zhuang, *ACS Appl. Energy Mater.* **2021**, *4*, 2891-2898.

[21] a) M. Shelby, P. Lestrange, N. Jackson, K. Haldrup, M. Mara, A. Stickrath, D. Zhu, H. Lemke, M. Chollet, B. Hoffman, *J. Am. Chem. Soc.* **2016**, *138*, 8752-8764; b) L. Chen, X. Zhang, E. Wasinger, K. Attenkofer, G. Jennings, A. Muresan, J. Lindsey, *J. Am. Chem. Soc.* **2007**, *129*, 9616-9618.

[22] A. Harutyunyan, A. Kuznetsov, *Chem. Phys. Lett.* **1995**, *241*, 168-172.

[23] Z. Gao, Z.-H. Zhao, H. Wang, Y. Bai, X. Zhang, Z. Zhang, H. Mei, M. Yuan, G. Zhang, *Angew. Chem. Int. Ed.* **2023**, *63*, e202318967.

10.1002/anie.202506845

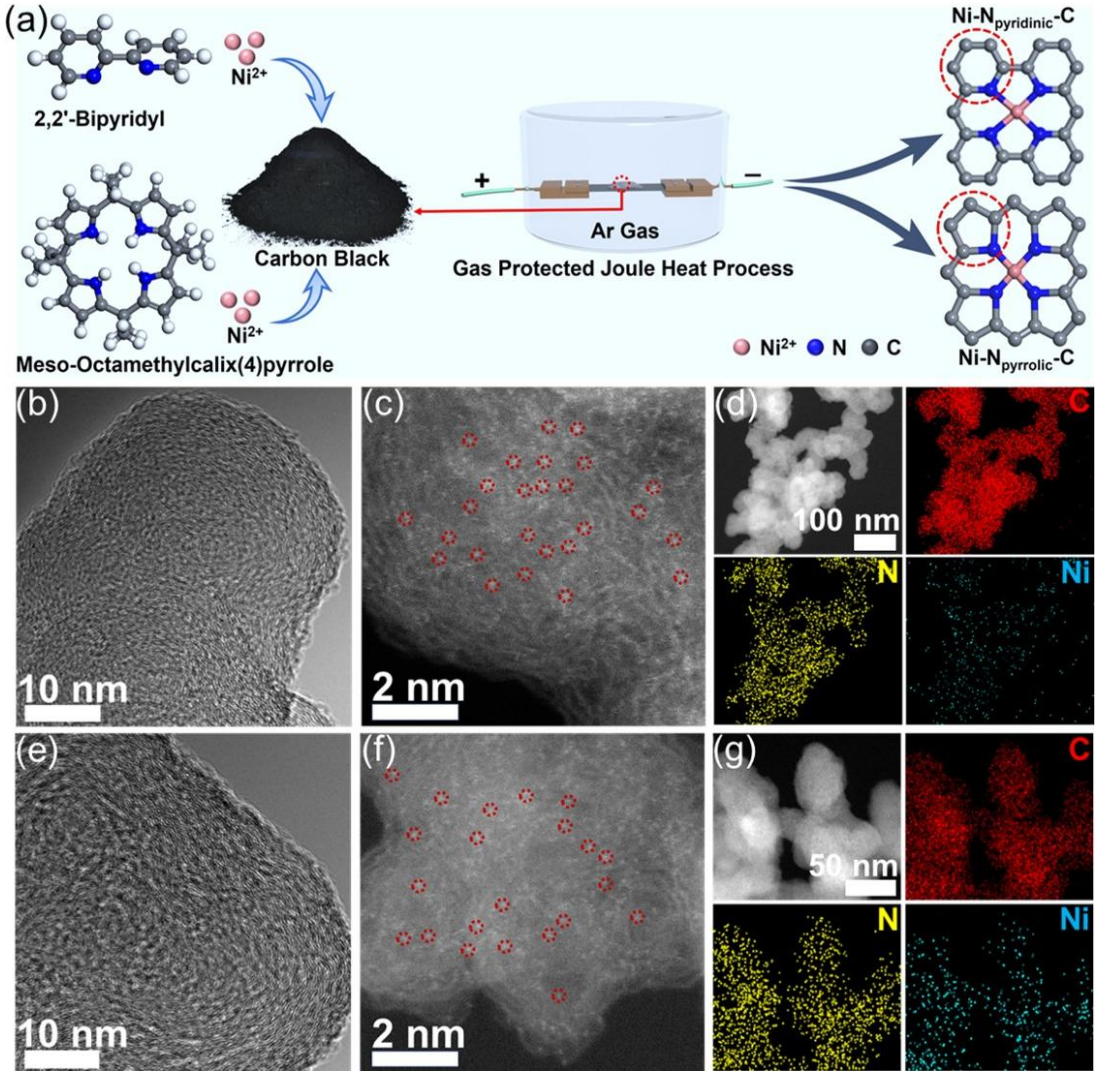

Figure 1. (a) Schematic illustration of the synthetic procedure of Ni-$N_{pyrrolic}$-C and Ni-$N_{pyridinic}$-C. (b) TEM image, (c) HAADF-STEM image and (d) elemental mapping images of Ni-$N_{pyridinic}$-C. (e) TEM image, (f) HAADF-STEM image and (g) elemental mapping images of Ni-$N_{pyrrolic}$-C.

10.1002/anie.202506845

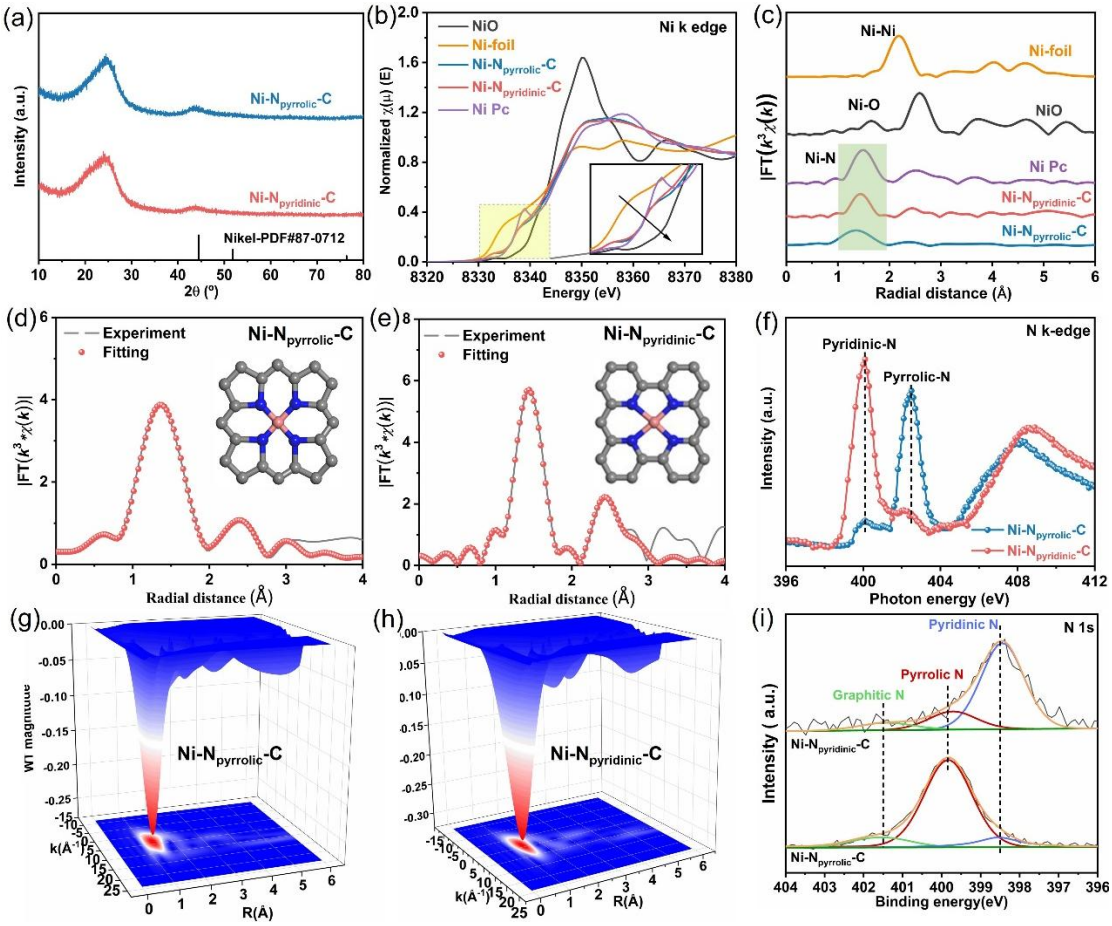

Figure 2. (a) XRD patterns of Ni-$N_{pyridinic}$-C and Ni-$N_{pyrrolic}$-C. (b) Normalized Ni K-edge XANES spectra and (c) Fourier-transform k^3-weighted EXAFS spectra of Ni K-edge for Ni-$N_{pyrrolic}$-C, Ni-$N_{pyridinic}$-C and corresponding references. (d-e) FT-EXAFS fitting results of Ni K-edge for Ni-$N_{pyrrolic}$-C and Ni-$N_{pyridinic}$-C shown in R-space. The data are k^3 weighted and not phase corrected. (f) XAFS spectra of N K-edge for Ni-$N_{pyrrolic}$-C and Ni-$N_{pyridinic}$-C. (g-h) Wavelet transforms for the k^2-weighted Ni K-edge EXAFS spectra for Ni-$N_{pyrrolic}$-C and Ni-$N_{pyridinic}$-C. (i) N 1s XPS spectra for Ni-$N_{pyrrolic}$-C and Ni-$N_{pyridinic}$-C.

10.1002/anie.202506845

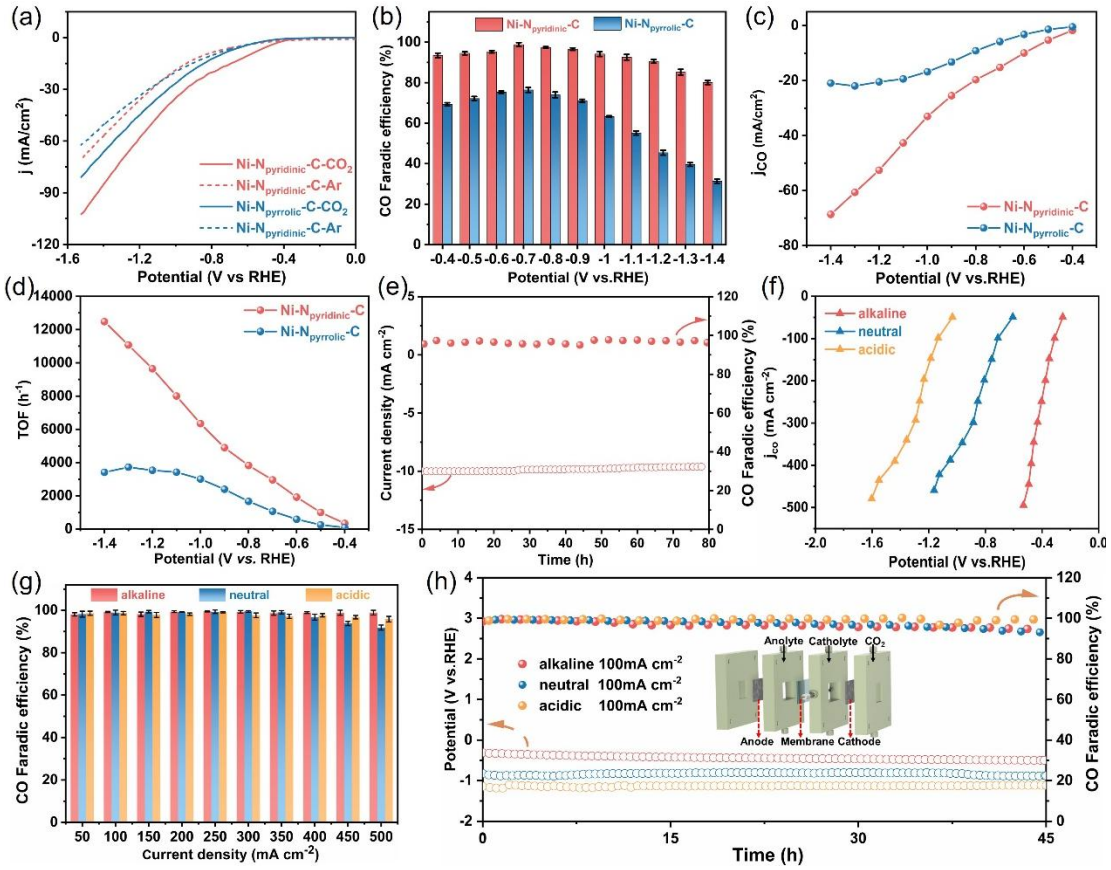

Figure 3. (a) LSV curves of Ni-$N_{pyrrolic}$-C and Ni-$N_{pyridinic}$-C in CO_2/Ar saturated electrolyte. (b) CO Faradaic efficiency and (c) CO partial current density of Ni-$N_{pyrrolic}$-C and Ni-$N_{pyridinic}$-C in H-cell. (d) TOF values of Ni-$N_{pyrrolic}$-C and Ni-$N_{pyridinic}$-C. (e) Stability test of Ni-$N_{pyridinic}$-C in H-cell for 80 hours. The electrolyte is 0.5 M $KHCO_3$. (f) CO partial current density and (g) CO Faradaic efficiency of Ni-$N_{pyridinic}$-C in Flow-cell with alkaline, neutral and acidic eletrolytes. (h) Durability test of Ni-$N_{pyridinic}$-C in Flow-cell and schematic illustration of gas-diffusion Flow-cell. The electrolyte are 1 M KOH (alkaline, pH=14), 0.05 M H_2SO_4 + 1M KCl (acidic, pH=1) and 1 M $KHCO_3$ (neutral, pH=8.2).

10.1002/anie.202506845

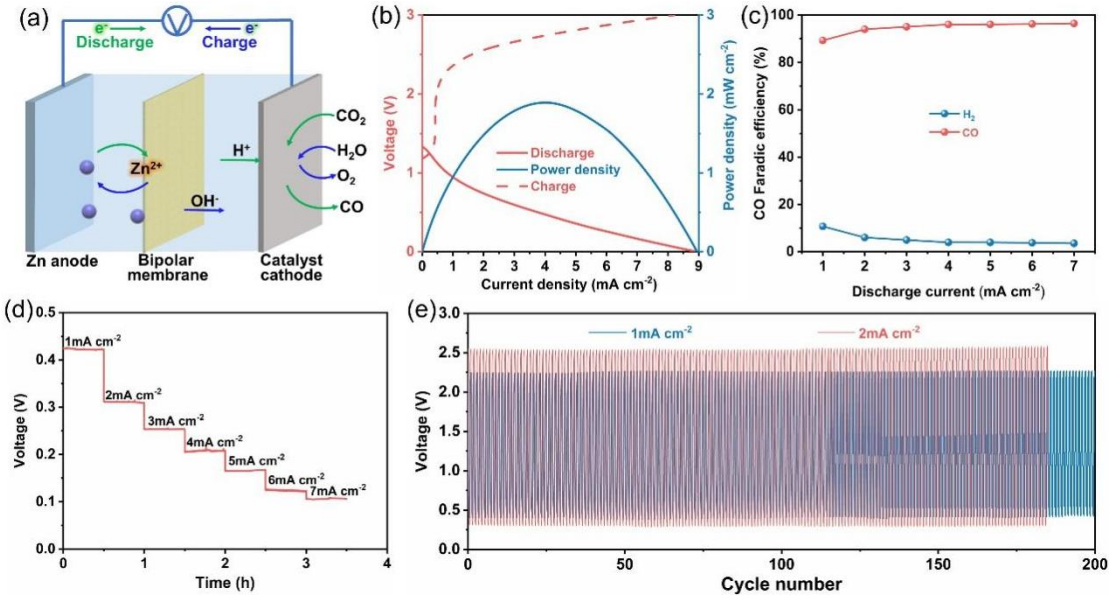

Figure 4. (a) Schematic illustration of a primary aqueous Zn-CO_2 battery. (b) Polarization curves and power density of Zn-CO_2 battery with Ni-$N_{pyridinic}$-C as electrocatalyst. (c) CO and H_2 Faradaic efficiency during discharge. (d) Discharge curves at different current densities. (e) Charge-discharge curves at different current densities.

10.1002/anie.202506845

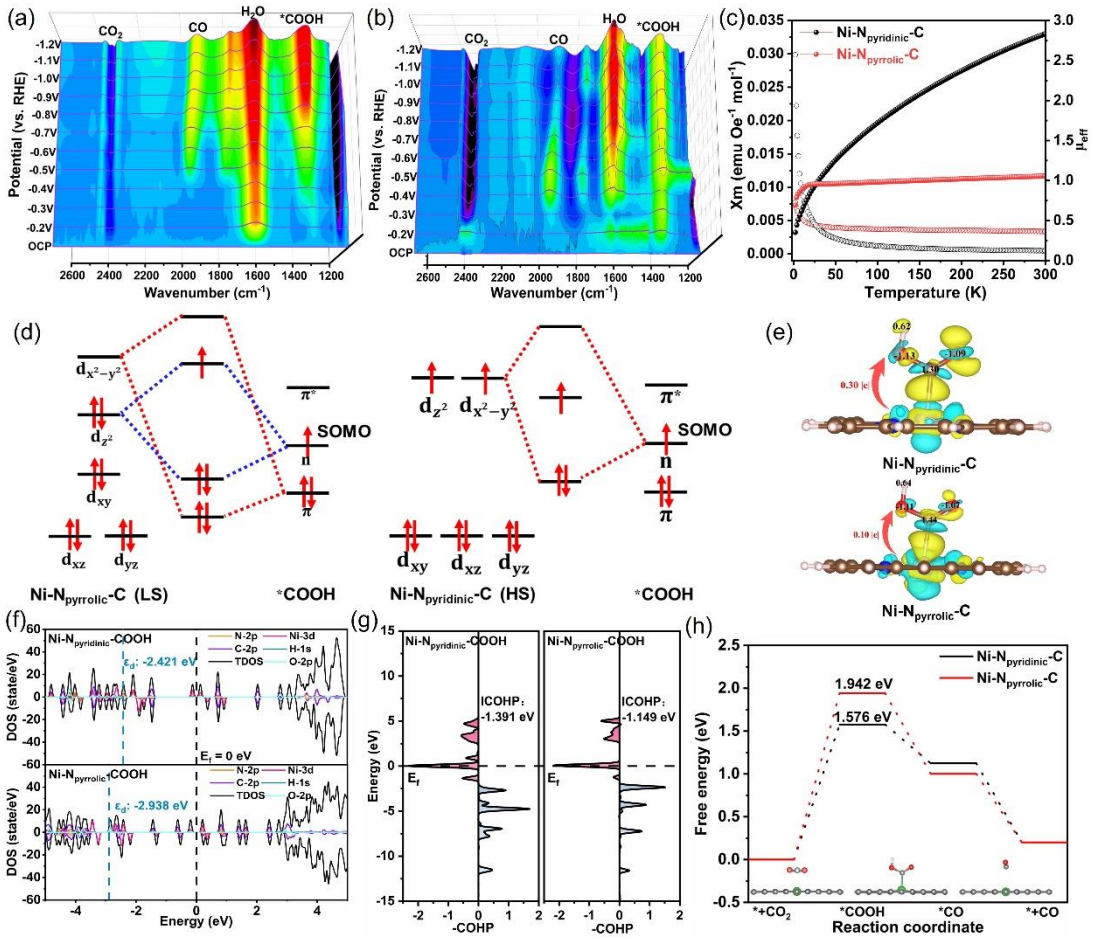

Figure 5. The *in-suit* ATR-FTIR spectra of CO_2 reduction on (a) Ni-$N_{pyridinic}$-C and (b) Ni-$N_{pyrrolic}$-C catalysts. (c) Magnetic susceptibility of Ni-$N_{pyridinic}$-C and Ni-$N_{pyrrolic}$-C. (d) Orbital interactions between *COOH and Ni over Ni-$N_{pyrrolic}$-C (LS) and Ni-$N_{pyridinic}$-C (HS). (e) Charge density difference and Bader charge analysis of *COOH adsorbed on Ni-$N_{pyridinic}$-C and Ni-$N_{pyrrolic}$-C. (f) Projected density of states of Ni and *COOH over Ni-$N_{pyridinic}$-C and Ni-$N_{pyrrolic}$-C. (g) COHP analysis of Ni-COOH over Ni-$N_{pyridinic}$-C and Ni-$N_{pyrrolic}$-C. (h) Free energy profiles of CO_2RR on Ni-$N_{pyridinic}$-C and Ni-$N_{pyrrolic}$-C.

10.1002/anie.202506845

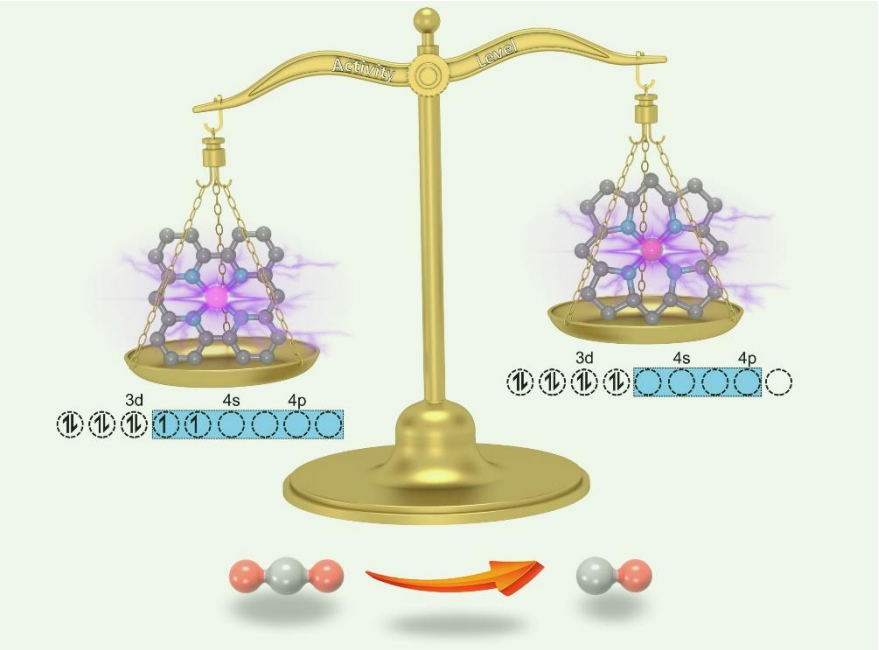

Two well-designed Ni-N_4C single atom electrocatalysts with dfferent coordinated nitrgen species have been developed via a gas-protected fast joule heating strategy. The pyridinic-type nitrogen coordinated Ni-$N_{pyridinic}$-C exhibits a superior electrocatalytic activity than the pyrrolic-type nitrogen coordinated Ni-$N_{pyrrolic}$-C for CO_2 reduction in H-type cell, with nearly 100% Faradaic efficiency for CO. Remarkedly, excellent catalytic activities also achieve in all alkaline, neutral and acidic electrolytes with industrial-level CO partial current densities. The outstanding durability and CO selectivity origin from modulating the spin-state of Ni center with different coordinated-N species, which significantly strengthen the interaction and faciliate the electron transfer between Ni center and *COOH intermediate, leading to the decreased energy barrier for *COOH formation and boosted reaction kinetics for *COOH further reduction.